Acta Cryst A FOUNDATIONS ADVANCES

ISSN 2053-2733

Atomic scale analyses of $\mathbb{Z}$-module defects in an NiZr alloy

Abdullah Sirindil,[a] Raphael Kobold,[b] Frédéric Mompiou,[c] Sylvie Lartigue-Korinek,[d] Loic Perriere,[d] Gilles Patriarche,[e] Marianne Quiquandon[a] and Denis Gratias[a]*

[a]CNRS-Laboratoire de Métallurgie de l'UMR 8247, IRCP Chimie-ParisTech, 11 rue Pierre et Marie Curie, 75005 Paris, France, [b]Institute of Material Physics in Space, German Aerospace Center (DLR) Linder Höhe, 51170 Cologne, Germany, [c]CNRS-CEMES and Université de Toulouse, 29 rue Jeanne Marvig, 31055 Toulouse, France, [d]CNRS-ICMPE UMR 7182 CNRS-UPEC, 2-8 rue Henri Dunant, 94320 Thiais, France, and [e]CNRS-C2N – Marcoussis UMR 9001, Route de Nozay, 91460 Marcoussis, France. *Correspondence e-mail: denis.gratias@chimie-paristech.fr

Received 8 June 2018
Accepted 10 August 2018

Edited by K. Tsuda, Tohoku University, Japan

Keywords: $\mathbb{Z}$-module; defects; twins; dislocations; HREM-HAADF.

Some specific structures of intermetallic alloys, like approximants of quasicrystals, have their unit cells and most of their atoms located on a periodic fraction of the nodes of a unique $\mathbb{Z}$-module [a set of the irrational projections of the nodes of a ($N > 3$-dimensional) lattice]. Those hidden internal symmetries generate possible new kinds of defects like coherent twins, translation defects and so-called module dislocations that have already been discussed elsewhere [Quiquandon *et al.* (2016). *Acta Cryst.* A**72**, 55–61; Sirindil *et al.* (2017). *Acta Cryst.* A**73**, 427–437]. Presented here are electron microscopy observations of the orthorhombic phase NiZr – and its low-temperature monoclinic variant – which reveal the existence of such defects based on the underlying $\mathbb{Z}$-module generated by the five vertices of the regular pentagon. New high-resolution electron microscopy (HREM) and scanning transmission electron microscopy high-angle annular dark-field (STEM-HAADF) observations demonstrate the agreement between the geometrical description of the structure in five dimensions and the experimental observations of fivefold twins and translation defects.

1. Introduction

The present article is the experimental continuation of a search to identify possible new defects in structures where the atoms, in addition to being periodically distributed, are located on a long-range-ordered subset of the nodes of a $\mathbb{Z}$-module.

The phase diagram of the binary system (Ni, Zr) presents a congruent solidification point at 1533 K for the equiatomic composition $Ni_{50}Zr_{50}$ close to a eutectic transformation, on the Zr-rich side, with a precipitation of $Zr_{67}Ni_{33}$ at 1295 K. The equiatomic $Ni_{50}Zr_{50}$ phase has an orthorhombic structure which, as will be demonstrated later, has the very remarkable property of being fully described using one unique pentagonal $\mathbb{Z}$-module including both atomic species. This orthorhombic stoichiometric NiZr structure was first reported by Kirkpatrick *et al.* (1962) as a CrB-type structure and has a remarkable tendency to generate quinary twins. This feature has been discussed in depth in a general framework by Parthé (1976). The first direct observations of those twins by transmission electron microscopy (TEM) were performed by Jiang *et al.* (1985) and a few years later, in much more detail, by Bouzy *et al.* (1991). Very recently, an impressive experimental study of the morphology of slowly solidified samples cooled in a containerless electrostatic levitation furnace has revealed beautiful central twins forming an almost perfect decagon in

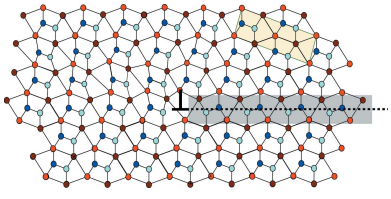

OPEN ACCESS

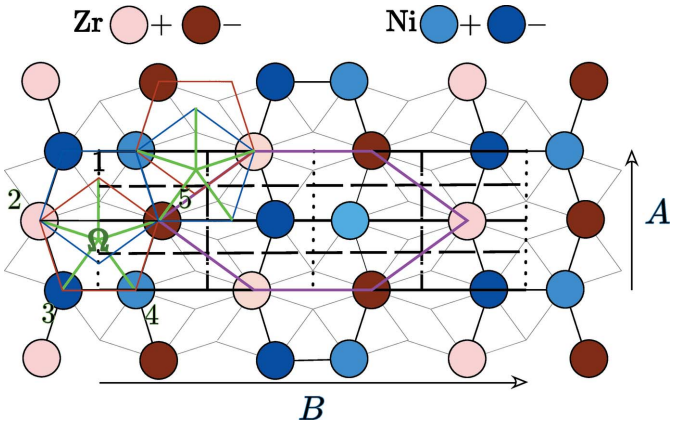

Figure 1
The NiZr structure (Kirkpatrick *et al.*, 1962) is a CrB-type structure *Cmcm* with lattice parameters $|A|$ = 0.3268, $|B|$ = 0.9973 and $|C|$ = 0.4101 nm, defined by two Wyckoff positions: Ni at (0, 0.0817, 1/4) and Zr at (0, 0.3609, 1/4). Ni and Zr atoms projected in the [001] plane form hexagons that are the superimposition of two opposite regular pentagons (in red and blue in the figure) sharing the same diagonal with an accuracy better than 1%. The symbols + and − correspond to the z coordinates being equal, respectively, to 1/4 and −1/4. The two usual tiles of the Penrose tiling (rhombi of acute angles $\pi/10$ and $\pi/5$) are outlined in light grey. All atomic positions belong to the $\mathbb{Z}$-module generated by the five vectors in green noted from 1 to 5. The structure can advantageously be described as a tiling of a unique equilateral hexagonal prototile drawn in purple (see Fig. 3).

solidified spherical samples, as observed by scanning electron microscopy (SEM), energy-dispersive X-ray spectroscopy (EDS) and electron backscatter diffraction (EBSD) (Hornfeck *et al.*, 2014).

2. Embedding the NiZr orthorhombic (monoclinic) phase in five dimensions

After Kirkpatrick *et al.* (1962), the orthorhombic phase NiZr has the space group *Cmcm* with lattice parameters $|A|$ = 0.3268, $|B|$ = 0.9973 and $|C|$ = 0.4101 nm. It is defined by two Wyckoff positions 4*c* *m*2*m* (0, y, 1/4) with $y_{\rm Ni}$ = 0.0817 and $y_{\rm Zr}$ = 0.3609 as shown in Fig. 1.

All Ni and Zr atoms are distributed along the z direction at locations ±1/4. It is thus possible, with no loss of information, to characterize this z coordinate by a simple two-valued symbol ± analogous to an internal scalar spin parameter.

Considering the two remaining coordinates (x, y), the fundamental point to emphasize is that the hexagons observed on the projection of the structure along the direction [0, 0, 1] are very close[1] to the hexagons that are obtained by superimposing two opposite regular pentagons sharing the same diagonal[2] as shown in Fig. 1. Because of this very specific internal geometry of the hexagons and the way they are connected in rows, the resulting projected two-dimensional structure can be entirely described using the node positions of the five-dimensional regular primitive hypercubic lattice where the five basic vectors project along the vertices of a regular pentagon. This is made clear in Fig. 1 where a tiling is drawn in the background in light grey based on the two basic prototiles (rhombi of acute angles $\pi/10$ and $\pi/5$) of the famous Penrose tiling (Penrose, 1979): all atoms are located on certain nodes of this tiling. Therefore, and very similarly to the case of quasicrystals (see Shechtman *et al.*, 1984), this allows us to reformulate the ideal structure of NiZr by embedding it in a five-dimensional space using atomic positions with five indices for the (x, y) description, in addition to the scalar two-valued spin-like index ± representing the z coordinate ±1/4. This new configurational five-dimensional Euclidian space corresponding to the (x, y) plane decomposes as

$$R^5 = R^2_{\parallel} \oplus R^2_{\perp} \oplus R_{\Delta}$$

where R_{Δ} is the one-dimensional line along the main diagonal (1, 1, 1, 1, 1) in five-dimensional space. This is the standard way of generating the Penrose tiling using the cut-and-project method [see for instance Duneau & Katz (1985), Kalugin *et al.* (1985), Elser (1986)].

The five indices are unambiguously determined up to any five-dimensional translation along the main diagonal $\Delta = (1, 1, 1, 1, 1)$. For simplicity and with no loss of generality, we choose to gather all atomic positions in a unique and the same four-dimensional plane perpendicular to Δ: the actual atomic positions V of NiZr can thus be expressed as $V = (n_1, n_2, n_3, n_4, n_5; \pm)$, with $\sum_{i=1}^{5} n_i$ = Const.

As easily seen in Fig. 1, the two-dimensional (x, y) unit cell of NiZr is defined by the five-dimensional vectors $A = (0, 1, \overline{1}, \overline{1}, 1)$ and $B = (0, \overline{3}, \overline{1}, 1, 3)$, both perpendicular to Δ. Because of its C character, the two-dimensional lattice generated by A and B in five dimensions, say $L_{\parallel}$, is defined by

$$\begin{aligned} L_{\parallel} &= n(A + B)/2 + m(A - B)/2 \\ &= (0, 2m - n, -n, -m, 2n - m),\ n, m \in \mathbb{Z}. \end{aligned}$$

The structure itself is defined by four translation orbits[3] satisfying the (arbitrary) condition $\sum n_i$ = Const. = 1, irrespective of the point symmetry elements:

$$\begin{aligned} \text{NiZr} := \{&(0, 1, 0, 0, 0; +)_{\rm Zr}, (0, 0, 0, 0, 1; -)_{\rm Zr}, \\ &(0, 0, 1, 0, 0; -)_{\rm Ni}, (0, 0, 0, 1, 0; +)_{\rm Ni}\}\ L_{\parallel}. \end{aligned}$$

The five-dimensional symmetry elements are written as usual as $\widehat{g} = (g|t)$ where t is the associated five-dimensional translation and g is the point symmetry operation economically written as signed permutations $p(e_i)$ of the five unit vectors in five dimensions and a simple multiplication ±1 for the standard z coordinate:

$$\widehat{g} = (g|t) = (\{p(e_1), p(e_2), p(e_3), p(e_4), p(e_5); \pm 1\}|t).$$

[1] The accuracy of this ideal description is given by the ratio of the lattice parameters $|a|/|b| = 0.3268/0.9973 = 0.3277$ instead of the ideal value $\tan \pi/10 \simeq 0.3249$ for perfect regular pentagons; this gives an accuracy with respect to the ideal model better than 1%.

[2] In that regular pentagonal scheme, the ideal positions should be $y_{\rm Ni} = 1/(6\tau + 2) = (3\tau - 4)/10 = 0.08541$ instead of 0.0817 and $y_{\rm Zr} = (2\tau + 1)/(6\tau + 2) = (2 + \tau)/10 = 0.3618$ instead of 0.3609.

[3] The translation orbit of a point $\mathbf{v}$ is the subset of its equivalent points that can be written as $\mathbf{v}' = \mathbf{v} + \mathbf{T}$ where $\mathbf{T}$ is a translation of the lattice, irrespective of the point symmetry of the crystal.

For example the c mirror perpendicular to B in *Cmcm* transforms e_1 into itself, e_2 into e_5 and *vice versa*, e_3 into e_4 and *vice versa*, and adds $\frac{1}{2}$ to the z coordinate thus transforming $\frac{1}{4}$ (symbol +) into $-\frac{1}{4}$ (symbol −) and *vice versa*, corresponding for the scalar component to a multiplication by −1. It can therefore be written as $\widehat{m}_B = (\{1, 5, 4, 3, 2; \overline{1}\}|0, 0, 0, 0, 0)$ after choosing the point Ω in Fig. 1 as origin. Similarly, the mirror perpendicular to A can be written $\widehat{m}_A = (\{\overline{1}, \overline{5}, \overline{4}, \overline{3}, \overline{2}; 1\}|0, 1, 0, 0, 1)$. Finally, the mirror perpendicular to C and passing through $z = 1/4$ reduces to the identity in the present five-dimensional representation: $\widehat{m}_C = \mathrm{Id} = (\{1, 2, 3, 4, 5; 1\}|0, 0, 0, 0, 0)$.

Thus, the orthorhombic NiZr structure can be described using a subset of a Penrose tiling using the two rhombi of acute angles $\pi/10$ and $\pi/5$. As defined in a previous article (Sirindil *et al.*, 2017) we call this kind of structure a $\mathbb{Z}$-module-based alloy.

2.1. Elementary five-dimensional geometry

Starting from a five-dimensional node $(n_1, n_2, n_3, n_4, n_5)$, we obtain its components $(x_\parallel, y_\parallel)$ in the physical space $E_\parallel = R^2_\parallel$ and its three components $(x_\perp, y_\perp, z_\perp)$ in the complementary space $E_\parallel = R^2_\perp \oplus R_\Delta$ according to the following usual formulas (see, for instance, Duneau & Katz, 1985) using $\varphi = 2\pi/5$:

$$\begin{cases} x_\parallel = \left(\frac{2}{5}\right)^{1/2}(n_1 + n_2\cos\varphi + n_3\cos 2\varphi + n_4\cos 2\varphi + n_5\cos\varphi) \\ \quad = \frac{1}{10^{1/2}}(2n_1 + (h - h')\tau - h) \\ y_\parallel = \left(\frac{2}{5}\right)^{1/2}(n_2\sin\varphi + n_3\sin 2\varphi - n_4\sin 2\varphi - n_5\sin\varphi) \\ \quad = \left(\frac{3-\tau}{10}\right)^{1/2}(k + k'\tau) \\ x_\perp = \left(\frac{2}{5}\right)^{1/2}(n_1 + n_2\cos 2\varphi + n_3\cos\varphi + n_4\cos\varphi + n_5\cos 2\varphi) \\ \quad = \frac{1}{10^{1/2}}(2n_1 + (h' - h)\tau - h') \\ y_\perp = \left(\frac{2}{5}\right)^{1/2}(n_2\sin 2\varphi - n_3\sin\varphi + n_4\sin\varphi - n_5\sin 2\varphi) \\ \quad = \left(\frac{3-\tau}{10}\right)^{1/2}(k' - k\tau) \\ z_\perp = \left(\frac{1}{5}\right)^{1/2}(n_1 + n_2 + n_3 + n_4 + n_5) \\ \quad = \frac{1}{5^{1/2}}(n_1 + h + h') \end{cases} \tag{1}$$

with $\tau = (1 + 5^{1/2})/2$, $h = n_2 + n_5$, $h' = n_3 + n_4$, $k = n_3 - n_4$, $k' = n_2 - n_5$ and using

$$\cos\varphi = (\tau - 1)/2,\ \sin\varphi = (\tau + 2)^{1/2}/2,$$
$$\cos 2\varphi = -\tau/2,\ \sin 2\varphi = (3 - \tau)^{1/2}/2 = (\tau - 1)\sin\varphi.$$

To generate the orthorhombic NiZr structure, we apply a shear of the five-dimensional lattice Λ along $R^2_\perp$ – keeping R_Δ invariant – in such a way as to align two independent nodes of Λ along $R^2_\parallel$ by the transformation (see Jarić & Mohanty, 1987; Gratias *et al.*, 1995):

$$\begin{cases} x'_\parallel = x_\parallel \\ x'_\perp = x_\perp - \hat{\varepsilon}x_\parallel \end{cases}. \tag{2}$$

This will generate a two-dimensional lattice in $R^2_\parallel$. Taking A and B, the two five-dimensional vectors, the projections of which in $R^2_\parallel$ define the unit cell of the structure, we ensure the generated structure is periodic of periods $[A_\parallel, B_\parallel]$ by applying the shear matrix $\widehat{\varepsilon}$ such that $[A_\perp, B_\perp] - \widehat{\varepsilon}[A_\parallel, B_\parallel] = 0$ and therefore $\widehat{\varepsilon} = [A_\perp, B_\perp][A_\parallel, B_\parallel]^{-1}$.

Using $A = (0, 1, \overline{1}, \overline{1}, 1)$ and $B = (0, \overline{3}, \overline{1}, 1, 3)$, we obtain

$$[A_\parallel, B_\parallel] = \frac{1}{10^{1/2}}\begin{pmatrix} 4\tau - 2 & 0 \\ 0 & -(6 + 2\tau)(3 - \tau)^{1/2} \end{pmatrix}$$

and

$$[A_\perp, B_\perp] = \frac{1}{10^{1/2}}\begin{pmatrix} 2 - 4\tau & 0 \\ 0 & (2\tau - 6)(3 - \tau)^{1/2} \end{pmatrix},$$

leading to

$$\widehat{\varepsilon} = \begin{pmatrix} -1 & 0 \\ 0 & 2\tau - 3 \end{pmatrix}. \tag{3}$$

Equations (1) and (2) together with the explicit expression (3) of $\widehat{\varepsilon}$ are all we need to fully handle the embedding of the NiZr three-dimensional structure into the five-dimensional superspace back and forth and generate all possible defects that keep the underlying $\mathbb{Z}$-module invariant in $E_\parallel$.

2.2. Construction of the atomic surfaces generating the orthorhombic NiZr structure

The definition of atomic surfaces for periodic structures has been discussed in a previous article (Sirindil *et al.*, 2017) where it has been shown that the simplest choice of atomic surfaces is to collect the Voronoi cells in $E_\perp = R^2_\perp \oplus R_\Delta$ centred on the projections in $E_\perp$ of the translation orbits defining the structure.

Here, the orthorhombic structure is generated by four translation orbits: $w_1 = (0, 1, 0, 0, 0)$, $w_2 = (0, 0, 1, 0, 0)$, $w_3 = (0, 0, 0, 1, 0)$ and $w_4 = (0, 0, 0, 0, 1)$ as shown in Fig. 2. Using relations (2) and (3), we note that the nodes $V = (n_1, n_2, n_3, n_4, n_5)$ of Λ project after shear in $E_\perp = R^2_\perp \oplus R_\Delta$ as

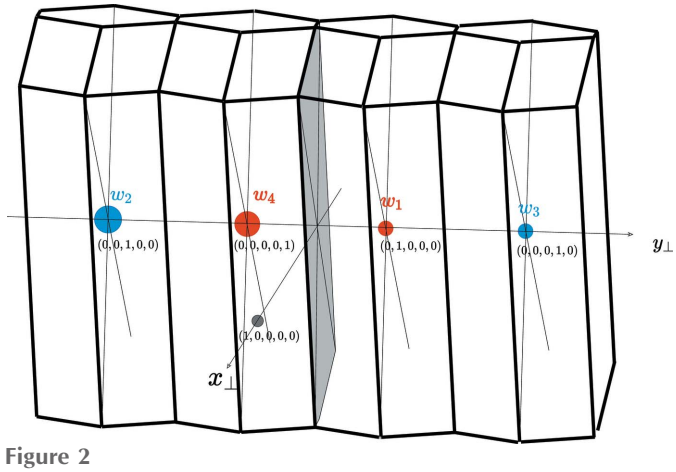

Figure 2
The four Voronoi cells in $E_\perp$ defining the atomic surfaces for the orthorhombic phase of NiZr are aligned along the $y_\perp$ direction. This very unusual situation suggests generating the structure using the hexagonal tile based on the three translations $t_1 = w_3 - w_1 = (0, \overline{1}, 0, 1, 0)$, $t_2 = w_4 - w_1 = (0, \overline{1}, 0, 0, 1)$ and $t_3 = w_4 - w_2 = (0, 0, \overline{1}, 0, 1)$, all three relating a Zr atom to another Zr atom.

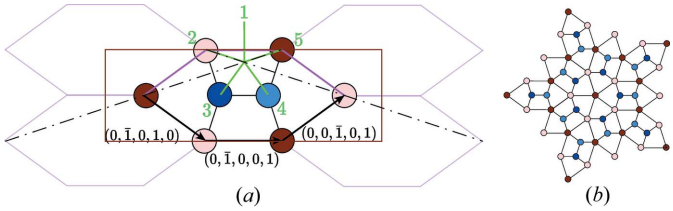

Figure 3
(*a*) The equilateral hexagonal prototile that generates the orthorhombic NiZr structure opens up a wide variety of possible tilings including the high-symmetry pentagonal snowflake (*b*). Whatever the tiling, all atoms apart from the unique central one in (*b*) share the same kind of environment to first neighbours as in the CrB reference structure. The set (*b*) describes the whole possible twins in the decomposition from $10mm'$ to $2mm'$: each variant can have two adjacent variants, obtained by a rotation $\pm\pi/5$ [or equivalently by a *c* mirror in the planes $(\pm1, 1, 0)$].

$$\pi_\perp V = \frac{1}{10^{1/2}} \begin{pmatrix} 4n_1 - n_2 - n_3 - n_4 - n_5 \\ (7-4\tau)^{1/2}(n_2 - 3n_3 + 3n_4 - n_5) \\ 2^{1/2}(n_1 + n_2 + n_3 + n_4 + n_5) \end{pmatrix}.$$

This makes the four translation orbits of the structure projecting in $E_\perp$ *four aligned points* along $y_\perp$ as shown in Fig. 2:

$$w_1 = \kappa(-1, (7-4\tau)^{1/2}, 2^{1/2}),\ w_2 = \kappa(-1, -3(7-4\tau)^{1/2}, 2^{1/2})$$
$$w_3 = \kappa(-1, 3(7-4\tau)^{1/2}, 2^{1/2}),\ w_4 = \kappa(-1, -(7-4\tau)^{1/2}, 2^{1/2})$$

with $\kappa = 1/10^{1/2}$.

This analysis suggests that the structure can also economically be viewed as a perfect tiling of a hexagonal prototile, as shown in Fig. 3(*a*), defined by the three vectors $t_1 = (0, \overline{1}, 0, 1, 0)$, $t_2 = (0, \overline{1}, 0, 0, 1)$ and $t_3 = (0, 0, \overline{1}, 0, 1)$ which generate the network of the Zr positions. Each of these hexagonal tiles is the very equivalent of a primitive unit cell. As will be shown later, the fact that the lengths of the three vectors t_1, t_2, t_3 are equal means that several kinds of tiling are equally possible, as exemplified in Fig. 3(*b*), with no change in the chemical species and atomic bonds of first neighbours. *This makes twinning the easiest defect process in this alloy*.

2.3. Symmetry breaking: the basic defect

The point symmetry of the four-dimensional lattice perpendicular to Δ which generates the $\mathbb{Z}$-module is $10mm'$ irrespective of the nature of the chemical species. Thus, the symmetry breaking induced by the perpendicular shear from $10mm'$ to $2mm'$ generates five twin variants issued from the coset decomposition:

$$10mm' = (\mathrm{Id} + m_2 + m_3 + m_4 + m_5)2mm'$$

where m_i designates the mirrors containing the ith vector defining the pentagon (in green in Fig. 3). Because of the *c* mirror of the structure, the variants are two-by-two equivalents: the mirrors m_2 and m_5 are in the $(1, 1, 0)$ and $(\overline{1}, 1, 0)$ planes whereas the mirrors m_3 and m_4 are in irrational planes with respect to the structure. Thus, a given variant can have only two different adjacent twins symmetric with respect to its *c* mirror. The atomic model of the twin operation is shown in

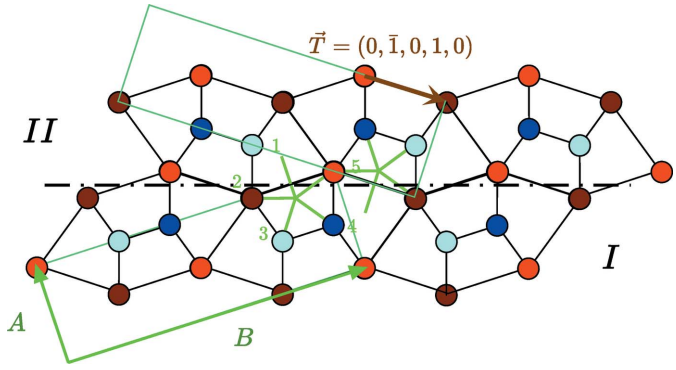

Figure 4
The simplest model of the structure of the quinary twin from the analysis in terms of $\mathbb{Z}$-module invariance as illustrated by the two pentagons in green. The twin operation $[\hat{\mathbf{m}}_{(110)}|(0, \overline{1}, 0, 1, 0)]$ is expressed in the *Cmcm* unit-cell coordinates.

Fig. 4. We choose the origin on the atomic Zr site number 5 in the figure. The twin point operation is the mirror defined by

$$m_{[110]} = \{3, 2, 1, 5, 4; -1\}.$$

The multiplication by -1 on the spin variable corresponds to the fact that to be coherent with respect to the tiling the mirror twin must transform $\pm$ symbols into $\mp$ implying thus an irreducible translation along *z* by $\pm1/2$.

The translation $\mathbf{t}$ associated with the twin in the (x, y) plane is shown in brown in Fig. 4 and is written $\mathbf{T} = (0, \overline{1}, 0, 1, 0)$. It decomposes into two parts: $\mathbf{T} = \mathbf{T}_\mathrm{i} + \mathbf{T}_\mathrm{r}$ where $\mathbf{T}_\mathrm{i}$ is the irreducible component independent of the choice of the origin and $\mathbf{T}_\mathrm{r}$ is the reducible part that vanishes by choosing the origin on the mirror:[4]

$$\mathbf{T}_\mathrm{i} = \frac{1}{4}(0, \overline{4}, 0, 2, 2),\ \mathbf{T}_\mathrm{r} = \frac{1}{2}(0, 0, 0, \overline{1}, 1).$$

In the standard *Cmcm* unit-cell coordinates, the irreducible translation, including the component along the *z* direction, is therefore

$$\mathbf{t}_\mathrm{i} = \frac{1}{4}[\overline{1}, 1, 0] + \frac{1}{2}[0, 0, 1] = \frac{1}{4}[\overline{1}, 1, 2]$$

which is identical to the irreducible translation proposed several years ago by Bouzy *et al.* (1991) based on a quite different approach. Because of the *C* lattice, translation $\mathbf{T}$ in Fig. 4 can equivalently be written as $\mathbf{T} = (0, 1, 0, 0, \overline{1})$ which translates into $\mathbf{t} = (0, 1/(2+\tau), 1/2)$ expressed on the unit cell of crystal I. As expected from the expression of the pentagonal projections (1), the *y* component of this translation is an irrational fraction of the lattice parameter *B*.

This basic mirror twin defect is remarkably coherent with respect to the atomic structure. Because the tiling of the elementary hexagons remains continuous at the level of the

[4] Any translation $\mathbf{t}$ associated with a point operation $\hat{\mathbf{g}}$ decomposes into a *reducible* part $\mathbf{t}_\mathrm{r}$ that can reduce to zero by an *ad hoc* choice of origin, and an invariant *irreducible* part $\mathbf{t}_\mathrm{i}$. This decomposition is particularly simple when $\hat{\mathbf{g}}$ is of order 2; $\hat{\mathbf{g}}^2 = \hat{\mathbf{1}}$, since then $\hat{\mathbf{g}}$ has eigenvalues ±1. Thus, $\mathbf{t}_\mathrm{i}$ is in the eigenspace associated with the eigenvalue +1 and $\mathbf{t}_\mathrm{r}$ in the one associated with the eigenvalue -1: $\hat{\mathbf{g}}\mathbf{t}_\mathrm{i} = \mathbf{t}_\mathrm{i}$, $\hat{\mathbf{g}}\mathbf{t}_\mathrm{r} = -\mathbf{t}_\mathrm{r}$.

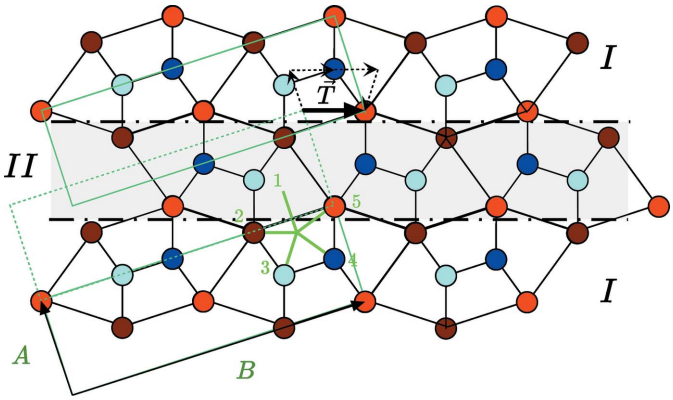

Figure 5
The simplest $\mathbb{Z}$-module translation defect model consists of introducing a thin slab of twinned hexagons (noted II) along a $(\bar{1}, 1, 0)$ plane. This generates an elementary translation between the upper and lower parts of crystal I of $\mathbf{T} = (1, \bar{2}, 1, 0, 0)$ (see the fine dotted arrows) corresponding to $\mathbf{t} = (2 - \tau)/2[\bar{1}, 1, 0]$ in the *Cmcm* unit cell.

interface, the chemical bonds between first neighbours are respected in all aspects, chemistry, lengths and angles between bonds. This makes this defect an excellent candidate to be actually observed in real crystals as will be shown next.

Translation boundaries are easily obtained by using two consecutive mirror twin defects. The thinnest translation defect is generated by inserting one single slab of twinned equilateral hexagons as shown in Fig. 5. The associated translation is $\mathbf{T} = (1, \bar{2}, 1, 0, 0)$ that is $\mathbf{t} = (2 - \tau)/2[\bar{1}, 1, 0]$ expressed in the *Cmcm* unit-cell coordinates. Of course, other global translation defects can be constructed using N slabs of twinned hexagons instead of one, leading thus to $\mathbf{T}_N = N(1, \bar{2}, 1, 0, 0)$ or $\mathbf{t}_N = N(2 - \tau)/2[\bar{1}, 1, 0]$.

Finally, we expect to observe the module dislocations that border the previous translation defect, *i.e.* module dislocations with a Burgers vector $\mathbf{B} = \mathbf{T} = (1, \bar{2}, 1, 0, 0)$ as shown in Fig. 6. This simple Burgers vector of the five-dimensional lattice takes an irrational value $\mathbf{b} = (2 - \tau)/2[\bar{1}, 1, 0]$ once expressed in the orthorhombic unit-cell coordinates. Observe that this dislocation is very special: as the translation defect is in fact a thin slab of a twinned crystal, the dislocation is the interface dislocation necessary to grow one step of a slab of a twinned individual in the other making it a so-called disconnection (see, for example, Hirth & Pond, 1996).

3. Sample preparation

In order to check the validity of our previous predictions from the $\mathbb{Z}$-module description, we prepared samples of NiZr for high-resolution TEM investigations in high-resolution electron microscopy (HREM) and scanning transmission electron microscopy high-angle annular dark-field (STEM-HAADF) modes. Samples used in the present study were obtained by two different methods:

(*a*) A first fusion under magnetic levitation of a mother alloy of nominal atomic composition $Ni_{44}Zr_{56}$, remelted and rapidly quenched by planar flow casting and annealed for one week at 973 K in sealed ampoules under vacuum.

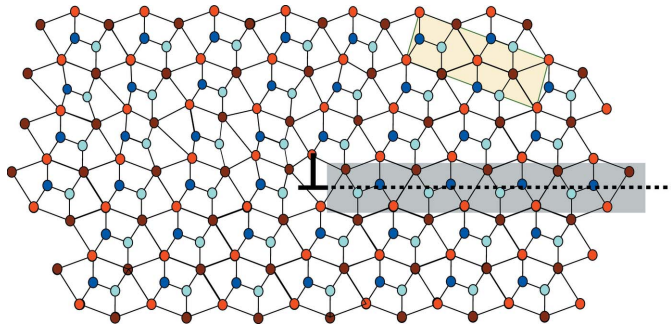

Figure 6
Simple sketch of the basic module dislocation with Burgers vector $\mathbf{B} = (1, \bar{2}, 1, 0, 0)$.

(*b*) High-purity elements [purity of Zr 99.97% (Smart Elements), Ni 99.995% (Alfa Aesar)] were prepared and alloyed by arc-melting at the DLR in Cologne (Germany) yielding a spherical sample of intermetallic NiZr with a diameter of 3 mm. Subsequently the sample was processed in an electrostatic levitation furnace (ESL)[5] under high vacuum conditions (10^{-5} Pa) in order to obtain a single homogeneous crystallization event at high undercoolings (ΔT = 300 K) and specific microstructural features as described by Hornfeck *et al.* (2014).

Samples (*a*) are roughly 300 µm-thick ribbons in which small discs of 3 mm in diameter are cut and polished. The characterization by X-ray powder diffraction has been performed on a Panalytical X'PERT Pro diffractometer using Co $K\alpha$ radiation with wavelength 0.17889 nm. The powder spectra reveal that the samples contain essentially the orthorhombic phase and a few per cent in volume of $NiZr_2$.

Concerning samples (*b*), since the orthorhombic phase grows in large multi-twinned grains with the [0,0,1] direction being clearly identifiable by sample surface features, these samples have been cut perpendicularly to the [0,0,1] direction and subsequently ground and polished until discs of about 150 µm remained. The highly accurate orientation of the samples makes the observations by HREM and STEM-HAADF particularly efficient: because of the strong induced texture, the orthorhombic phase grows in large multi-twinned grains with the direction [0,0,1] being the normal to the disc plane.

4. Electron microscopy analyses at atomic resolution

Samples (*a*) were thinned by mechanical grinding down to 100 µm and eventually thinned to electron transparency using

[5] A typical ESL processing cycle with NiZr consists of the following steps: the levitating sample is heated with an infrared laser (P = 75 W, λ = 808 nm) in order to melt the sample; the temperature of the melt is further increased by about 50 K above T_m in order to evaporate possible contaminants. The heating laser is turned off, the melt cools and eventually undercools below T_m only through radiation of heat, with a mean cooling rate of about 50 K s^{-1}; solidification sets in at ΔT = 300 K below T_m. A NiZr sample, which solidifies at such undercoolings, exhibits two distinctive poles on its surface, similar to a globe. In the sample interior these poles are connected by the crystallographic direction [0,0,1] (see Hornfeck *et al.*, 2014). With these surface features one has the opportunity to orient the spherical sample and cut it perpendicular to [0,0,1], which was realized with a custom-built orientation tool.

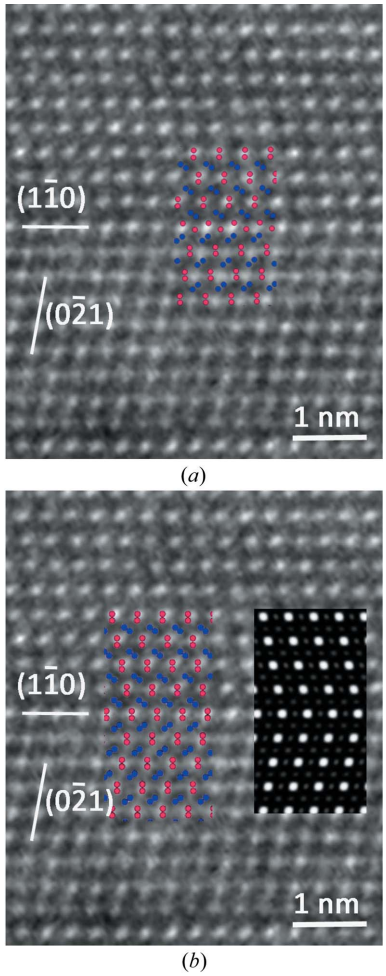

Figure 7
Quinary twin observed in HREM along the [112] direction with superimposition of the model $[\hat{\mathbf{m}}_{(110)}|0, 1/(2+\tau), z]$ expressed in the *Cmcm* unit-cell coordinates shown in Fig. 4 with $z = 0$ (*a*) and $z = 1/2$ (*b*). The distribution of white dots in the micrograph at the level of the interface is clearly in favour of the $z = 1/2$ solution.

ion milling (Gatan PIPS) until the formation of a hole. Samples (*b*) were electropolished using a Tenupol with a solution of 10% perchloric acid and 90% methanol at 243 K under 35 V.

Both samples (*a*) and (*b*) have been examined in HREM mode on two different machines: a Topcon 002B equipped with an LaB_6 cathode operating at 200 keV with a point-to-point resolution of 0.18 nm (ICMPE, Thiais, France) and a Hitachi 3300 electron microscope operating at 300 keV with $C_s \simeq 0$, $C_c = 3.7$ mm (CEMES, Toulouse, France). The STEM-HAADF and STEM bright-field (STEM-BF) observations have been performed on an FEI Titan Themis 200 [Center for Nanosciences and Nanostructures (C2N), Marcoussis, France]. This microscope uses an XFEG gun under 200 keV and is equipped with a C_s corrector (point-to-point resolution around 80 pm) and a CMOS CETA 4 k × 4 k camera. It can operate under various imaging STEM modes: BF and HAADF.

In both (*a*) and (*b*) samples, conventional BF TEM images show numerous defects, twins and translation boundaries.

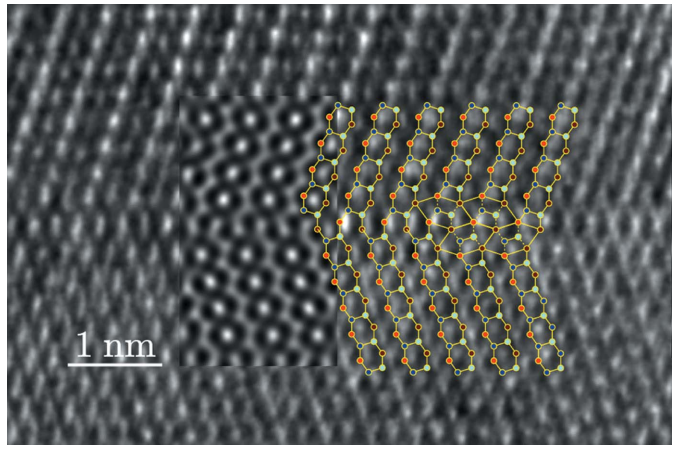

Figure 8
HREM image of a quinary twin observed along the [001] direction showing the translation associated with the mirror twin with the expected model and an insert of the image simulation made with the theoretical translation $\mathbf{T} = (0, \bar{1}, 0, 1, 0)$ of our model.

However, careful electron microscopy diffraction observations have shown in various locations of the samples a few additional low-intensity spots, like the one located at 1/2(1, 1, 1), that are typical of a second unexpected phase. We identified this low-temperature phase as a monoclinic deformation of the orthorhombic phase appearing below 473 K. It results from a small shift of the atomic positions along the *z* direction for both Ni and Zr, and is analogous to the phase discovered several years ago by Bendersky *et al.* (1996) in the (Pd,Zr) system. It is discussed in more detail in Appendix *A*.

4.1. Quinary twins

Quinary twins are very frequent in both samples (*a*) and (*b*) and quite easy to recognize. In order to make a full three-dimensional analysis of the associated translation, we made several HREM observations along the [112] direction to determine the translation part along the *z* direction. The result is seen in Fig. 7 together with the atomic simulations from our model with and without the 1/2 translation along *z*: it is clear that only the model with the $z = 1/2$ component corresponds to the experimental image.

In addition to these observations along the [112] direction, we performed HREM, STEM-BF and STEM-HAADF observations to determine the translation components in the [001] plane using samples (*b*). The HREM picture (CEMES) in Fig. 8 shows a clear translation associated with the mirror twin that fits quite well with the expected model of Fig. 4.

Observations at the ultimate resolution of atomic level in STEM-HAADF and STEM-BF modes performed on the same samples along the [001] direction fully confirm the model with a perfect agreement as shown in Fig. 9. The very comparable contrast variations at the level of the interface between the HAADF and BF micrographs prove that no significant displacements of the atomic positions occur at the boundary level owing to the remarkable crystalline coherency generated by the continuity of the tiling at the boundary crossing.

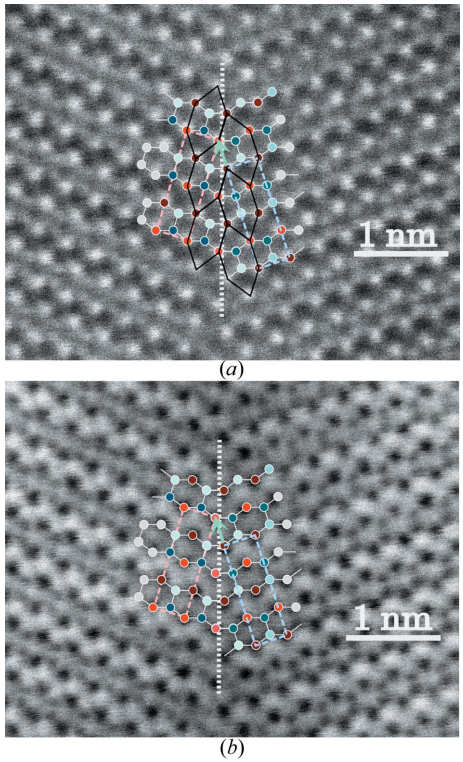

Figure 9
(*a*) STEM-HAADF atomic resolution of the quinary twin; (*b*) STEM-BF showing the remarkable invariance of the contrast on both sides of the boundary due to the very small local elastic field at the level of the boundary.

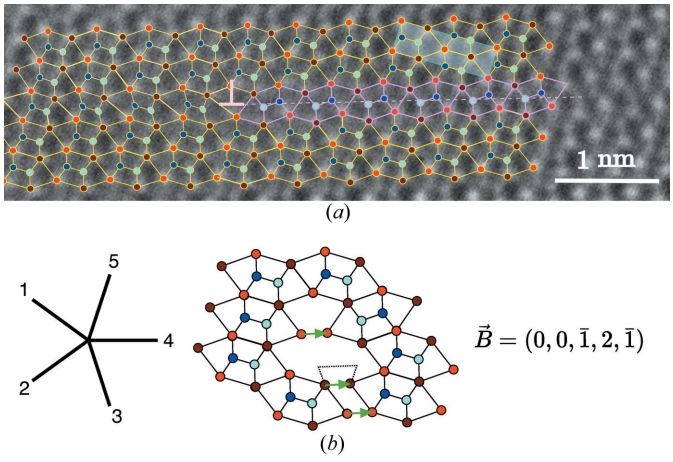

Figure 10
(*a*) HAADF observation of the elementary module dislocation defect in NiZr corresponding to the model of Fig. 6: the translation defect (in purple) with fault vector $\mathbf{T} = (0, 0, \bar{1}, 2, \bar{1})$ is bounded by the module dislocation with Burgers vector $\mathbf{B} = \mathbf{T}$. (*b*) Example of a circuit constructed on the $\mathbb{Z}$-module determining the Burgers vector $\mathbf{B} = (0, 0, \bar{1}, 2, \bar{1})$ consistent with the translation vector $\mathbf{T}$ of the corresponding planar fault.

4.2. Translation defects and module dislocations

Here, too, the prediction of the model has been fully experimentally verified: the only translation boundaries we could observe were those generated by a single slab of microtwin embedded in the crystal corresponding to the models in Figs. 5 and 6. This is exemplified on the HAADF

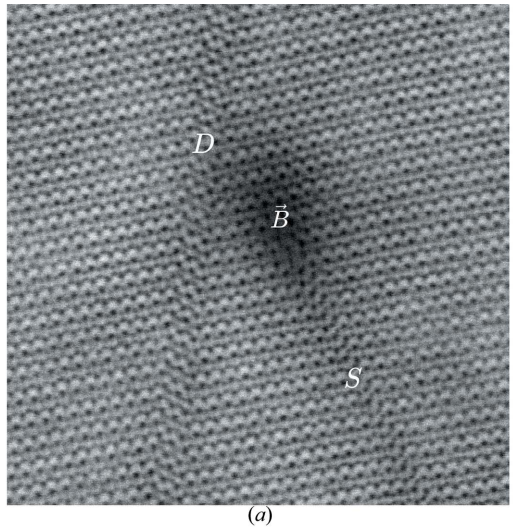

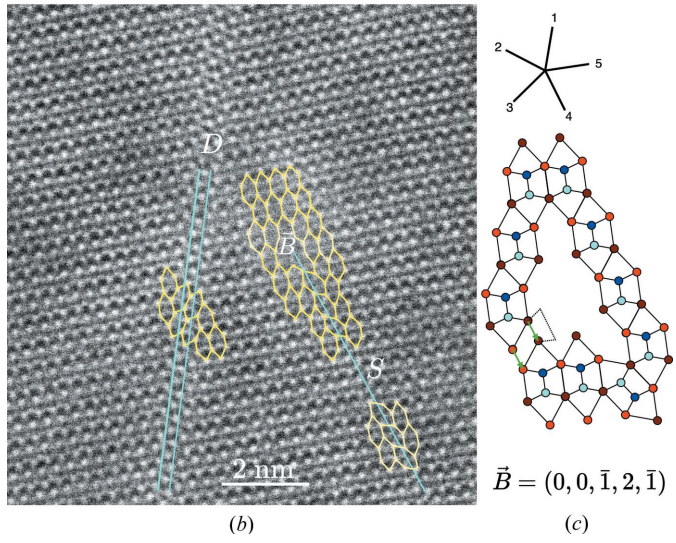

Figure 11
High-resolution STEM-BF (*a*) and STEM-HAADF (*b*) micrographs showing the two basic kinds of translation defects (*S* and *D*) and the elementary module dislocation *B*. The line noted *S* shows the simplest translation defects corresponding to the model in Fig. 5 made of one unique slab of hexagons with fault vector $\mathbf{T}_S = (0, 0, \bar{1}, 2, \bar{1})$. The double line *D* shows the translation defects generated with two slabs of hexagons $\mathbf{T}_D = 2 \times (2, \bar{1}, 0, 0, \bar{1})$. Finally, the dislocation *B* can be analysed using a simple generalization of Burgers circuit drawn in (*c*) leading, as expected, to a Burgers vector $\mathbf{B} = \mathbf{T}_S = (0, 0, \bar{1}, 2, \bar{1})$. As shown in (*a*), the translation defects generate almost no local deformation in contrast to the dislocation *B* which is surrounded by an observable displacement field generating the dark shadow extending for a few atomic distances.

micrograph of Fig. 10(*a*) which shows the planar translation of the fault vector $\mathbf{T} = (0, 0, \bar{1}, 2, \bar{1})$ defect on the right, with the module dislocation of the Burgers vector $\mathbf{b} = \mathbf{T}$ depicted in Fig. 10(*b*). The defect fits perfectly well with the simple theoretical model of Fig. 6.

The graphical way of determining the Burgers vector for an experimental picture is trivially achieved by reconstructing the very same sequence of undistorted hexagonal tiles as the one observed in the picture all around the defect and then measuring the closure default (in green in Fig. 10*b*).

We have analysed many defects on the various samples and have always found that their configurations can be decomposed using our three basic defects: quinary twin, translation boundary and the corresponding elementary module dislocation.

Fig. 11 shows at once three basic defects observed in both STEM-BF (*a*) and STEM-HAADF (*b*) modes. The translation boundary noted *S* is the exact experimental realization of the model of Fig. 5; the translation defect noted *D* is the two-slabs version of this defect. Finally, the localized defect noted *B* is the module dislocation that bounds the default *S*. A way of analysing this dislocation consists of drawing a close circuit of the basic hexagons around the defect (in yellow in Fig. 11*b*) and reproducing the very same circuit using ideal undeformed hexagons (see Fig. 11*c*): the closure defect is a direct measure of the Burgers vector. Here, we find $\mathbf{B} = (0, 0, \bar{1}, 2, \bar{1})$ which is, as expected, the value of the translation $\mathbf{T}$ associated with *S*.

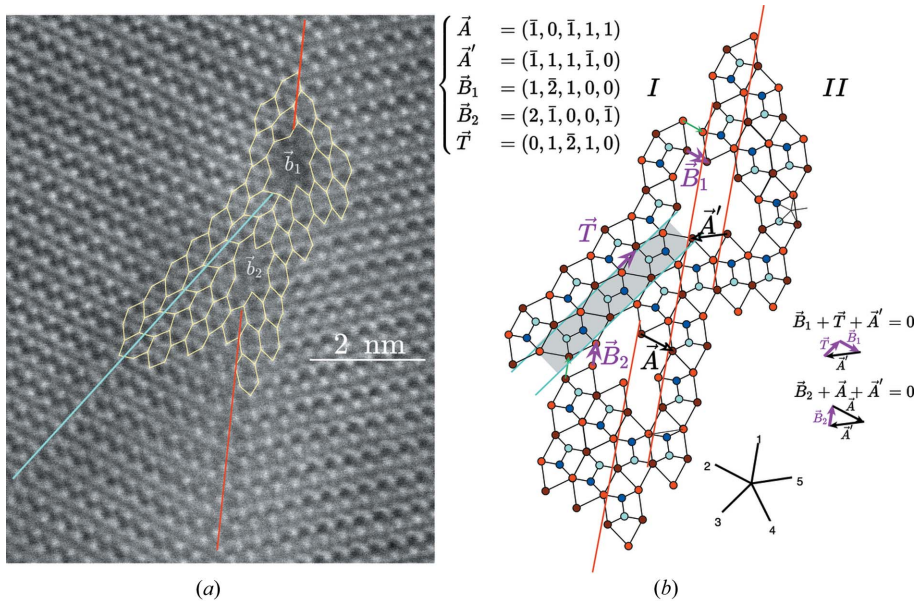

(*a*) (*b*)

Figure 12
Two module dislocations, a translation boundary and a quinary twin. The translation boundary is along the line drawn in blue, whereas the quinary twin interface is along the red line(s). The twin boundary is displaced by one step **A** or equivalently **A**′ at the level of each module dislocation.

Many other more complex configurations have been observed. For example, Fig. 12 shows a HAADF picture with two module dislocations, one translation defect (in blue) and quinary twins (in red). We note by **A** and **A**′ the unit vectors **a** in, respectively, crystal I and II: $\mathbf{A} = (\bar{1}, 0, \bar{1}, 1, 1)$ and $\mathbf{A}' = (\bar{1}, 1, 1, \bar{1}, 0)$. Having $\mathbf{T} = (0, 1, \bar{2}, 1, 0)$ and using the Burgers circuit on the module drawn in Fig. 12(*b*) we obtain $\mathbf{B}_1 = (1, \bar{2}, 1, 0, 0)$ and $\mathbf{B}_2 = (2, \bar{1}, 0, 0, \bar{1})$. It is thus easily verified that

$$\mathbf{B}_2 + \mathbf{A} + \mathbf{A}' = 0, \quad \mathbf{B}_1 + \mathbf{T} + \mathbf{A}' = 0.$$

These relations are consistent with the fact that the twin boundary is displaced by one step along **A**′ at the level of each module dislocation.

5. Discussion

All ultra-high-resolution HAADF or BF images presented in this study are various realizations of a *single-module* crystal in the sense that the entire observation areas are described on a unique $\mathbb{Z}$-module that is invariant everywhere on the picture: vectors relating any two (equivalent) white dots on the micrographs are integer linear combinations of the five pentagon unit vectors with constant sum.

Some module dislocations are located inside the crystals (see Fig. 10), others are located at the interfaces between twinned crystals like those of Fig. 12. In both cases, these dislocations are the same type of module dislocations with the same Burgers vector of type $\mathbf{B} = (\bar{1}, 2, \bar{1}, 0, 0)$ whatever their locations with respect to the other defects.

The use of $\mathbb{Z}$-modules in crystallography goes beyond solely structural aspects. In fact, any geometrical description that deals with more than one crystal as in the case of the geometry of grain boundaries [see for instance, Pond (1989) and Hirth & Pond (1996)] is naturally adapted to the use of $\mathbb{Z}$-modules as a basic description tool. For example, let Λ_1 and Λ_2 be the lattices of two adjacent crystals defined by the unit-cell vectors, respectively, A_i and A'_i, i running from 1 to 3. The natural module to consider is generated by the union $\mathcal{B} = \Lambda_1 \cup \Lambda_2$, also called a bilattice, that is the set of the points ζ such that

$$\mathcal{B} := \left\{ \zeta = \sum_{i=1}^{3} (n_i A_i + n'_i A'_i), \;\; n_i, n'_i \in \mathbb{Z} \right\}.$$

This module $\mathcal{B}$ has a rank N between 6 and 3 according to the relative orientation of the lattices Λ_1 and Λ_2. It is usually the optimized description of the bicrystal: an N-dimensional lattice representation that includes all possible kinds of defects that can be encountered in the study of the bicrystal.

However, in specific cases, this module might well not be the most appropriate to describe defects. Indeed, there are cases, as in NiZr, where the atomic structure itself is a decoration of a deeper hidden $\mathbb{Z}$-module generated by the N vectors $\{e_k\}$. In that case, the unit cells $\{A_k\}$ and $\{A'_k\}$ of the two lattices Λ_1 and Λ_2 can be expressed as integer linear combination of the N vectors e_k:

$$A_i = \sum_{k=1}^{N} p_{i,k} e_k; \quad A'_i = \sum_{k=1}^{N} p'_{i,k} e_k, \; i = 1, 2, 3$$

and thus

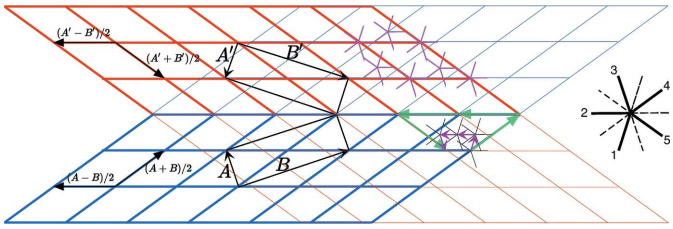

Figure 13
The bilattice $\mathcal{B}$, a module of rank 3 generated by the quinary twin in NiZr, is a subset of the pentagonal $\mathbb{Z}$-module. The basic module dislocation has Burgers vector $(\bar{1}, 2, \bar{1}, 0, 0)$ on the $\mathbb{Z}$-module (in purple) and $(1, 2, 1)$ (in green) on $\mathcal{B}$. Here, the pentagonal module allows for a finer description of the possible interface dislocations than the standard three-dimensional module defining the bilattice.

$$\mathcal{B} := \left\{ \zeta = \sum_{i=1}^{N} \sum_{i=1}^{3} (n_i p_{i,k} + n_i' p_{i,k}') e_k \;\; n_i, n_i' \in \mathbb{Z} \right\}. \qquad (4)$$

Thus, according to the values of the $p_{i,k}$ and $p_{i,k}'$, the set $\mathcal{B}$ may define only a fraction of the $\mathbb{Z}$-module.

For example, in the case of NiZr – and disregarding the direction z that is common to both twinned crystals – we have $A = (0, 1, \bar{1}, \bar{1}, 1)$, $B = (0, \bar{3}, \bar{1}, 1, 3)$ and $A' = (\bar{1}, 1, 0, 1, \bar{1})$, $B' = (\bar{1}, \bar{3}, 0, 3, 1)$ with a lattice of type C. The set $\mathcal{B}$ is thus defined by

$$\mathcal{B} = \{n(A + B)/2 + m(A - B)/2 + n'(A' + B')/2 + m'(A' - B')/2, n, m, n', m' \in \mathbb{Z}\}$$

or using equation (4) explicitly

$$\mathcal{B} = \{(-n', 2m + 2m' - n - n', -n, -m - m' + 2n', -m - m' + 2n)\}$$

with $n, m, n', m' \in \mathbb{Z}$. In the five-dimensional representation, this set of points is localized on a four-dimensional hyperplane perpendicular to the main five-dimensional diagonal $(1, 1, 1, 1, 1)$ (the sum of the five components is zero whatever the values of n, n', m and m'). It has rank 3 because $A - B = A' - B'$, so that dislocations in that framework are characterized by three integer indices only. *A general module dislocation of the five-dimensional description might well not be in the set* $\mathcal{B}$. Such is the case for the hypothetical dislocation of Burgers vector $\mathbf{B} = (1, 0, 0, 0, 0)$ that does not belong to $\mathcal{B}$. In contrast, the elementary dislocation of Burgers vector $\mathbf{B} = (\bar{1}, 2, \bar{1}, 0, 0)$ belongs to $\mathcal{B}$ with $n = n' = 1$, $m + m' = 2$, leading thus to $\mathbf{B} = (1, 2, 1)$ expressed in the three-dimensional module $\mathcal{B}$. The two approaches are sketched in Fig. 13.

6. Conclusion

This article is the experimental counterpart of a former one (Sirindil *et al.*, 2017) based on the idea of testing whether certain structures can be described in the context of $\mathbb{Z}$-modules, *i.e.* in high-dimension spaces, rather than in the standard framework based on three-dimensional lattices. We have shown here that the orthorhombic phase NiZr can be faithfully described in a five-dimensional space with high internal symmetry generating possible defects at the symmetry breaking induced by the projection back in the three-dimensional space. The ultra-high-resolution electron microscopy pictures have shown perfect agreement between observed and predicted defects. This set of experiments supports the use of $\mathbb{Z}$-modules in crystallography; this is indeed an interesting and fruitful unifying concept, even in direct space, where it is both an elegant formulation and an efficient tool to predict new possible defects including interface dislocations in structures with hidden non-crystallographic symmetries, in a unique mathematical framework.

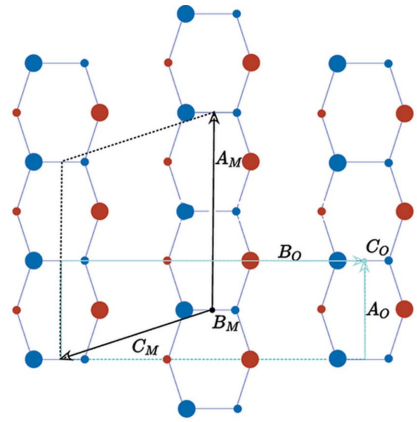

(*a*)

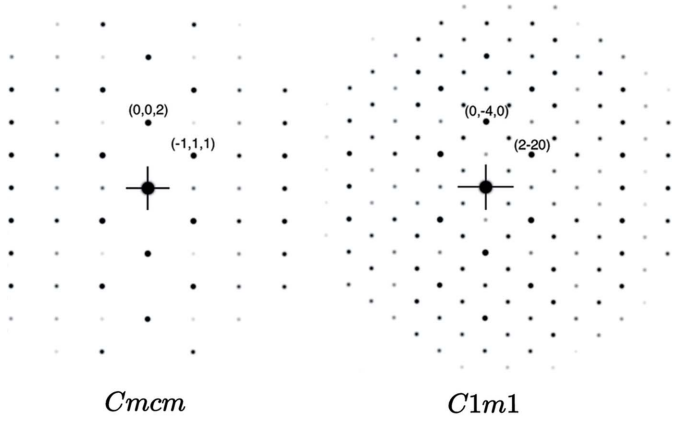

(*b*)

Figure 14
(*a*) The monoclinic $C1m1$ unit cell A_M, B_M, C_M, in black, and the orthorhombic $Cmcm$ A_O, B_O, C_O, in light blue. (*b*) Corresponding diffraction patterns for both structures.

APPENDIX A
The low-temperature monoclinic structure

We occasionally observed weak supplemental peaks at the positions 1/2(1, 1, 1) in the electron diffraction patterns with alternative strong and weak reflections typical of a slight deviation from the CrB-type ideal structure; this was demonstrated several years ago by Bendersky *et al.* (1996) in

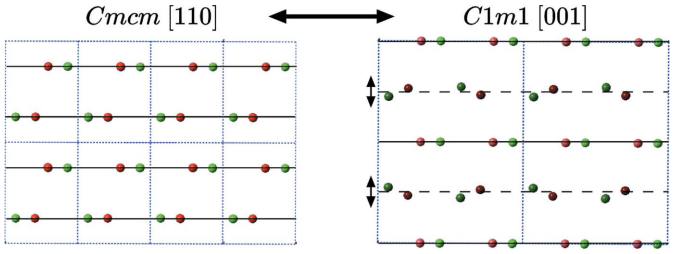

Figure 15
Ni are in red and Zr in green. In the monoclinic phase on the right, the atoms located on the glide mirror can move freely out of the mirror plane: the difference between the two structures consists of moving these atoms perpendicularly to the mirror.

the case of the (Pd,Zr) system which is very similar to (Ni,Zr). A transformation appears below 473 K towards a monoclinic variant with space group $C1m1$ as shown in Fig. 14. The results of our own crystallographic analysis corroborate and complete the remarkable analysis of Bendersky *et al.*. The monoclinic phase is characterized by the unit-cell parameter $\mathbf{A}_M$, $\mathbf{B}_M$ and $\mathbf{C}_M$ deduced from the orthorhombic parameters $\mathbf{A}_O$, $\mathbf{B}_O$ and $\mathbf{C}_O$ according to

$$\begin{cases} \mathbf{A}_M = 2\mathbf{A}_O \\ \mathbf{B}_M = 2\mathbf{C}_O \\ \mathbf{C}_M = -\frac{1}{2}(\mathbf{A}_O + \mathbf{A}_O) \end{cases} \quad \text{or} \quad \begin{cases} \mathbf{A}_O = \frac{1}{2}\mathbf{A}_M \\ \mathbf{B}_O = -\frac{1}{2}\mathbf{A}_M - 2\mathbf{C}_M \\ \mathbf{C}_O = \frac{1}{2}\mathbf{B}_M. \end{cases}$$

In reciprocal space, the relations are given by

$$\begin{cases} a_M^* = \frac{1}{2}(a_O^* + b_O^*) \\ b_M^* = \frac{c_O^*}{2} \\ c_M^* = 2b_O^* \end{cases} \quad \begin{cases} a_O^* = 2a_M^* - \frac{c_M^*}{2} \\ b_O^* = 2c_M^* \\ c_O^* = 2b_M^* \end{cases}$$

leading to the following relationships between the indices:

$$\begin{cases} h = \frac{H}{2} \\ k = \frac{H}{2} - 2L \\ l = \frac{K}{2} \end{cases} \quad \begin{cases} H = 2h \\ K = 2l \\ L = \frac{1}{2}(h - k) \end{cases}.$$

The lattice indices are given by the absolute value of the determinant of the unit-cell relationships:

$$i_{C(2A_O,2C_O,-1/2(A_O+B_O))/C(A_O,B_O,C_O)} = \det \begin{vmatrix} 2 & 0 & 0 \\ 0 & 0 & 2 \\ 1/2 & 1/2 & 0 \end{vmatrix} = 2$$

leading to the translation orbit decomposition (expressed on the *Cmcm* basis):

$$C(A_O, B_O, C_O) = \{(1|000) + (1|001)\} \times C(2A_O, 2C_O, -1/2(A_O + B_O))$$

and the point group decomposition:

$$m_x m_y m_z = (1 + m_x + m_y + 2_z)m_z$$

so that the complete basic coset decomposition for this transformation is written:

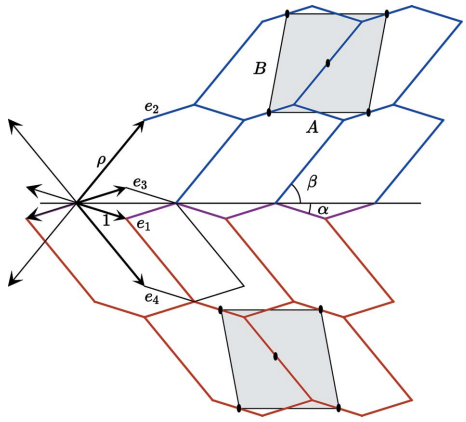

Figure 16
General coherent twin for structures defined by hexagons generated by $\mathbf{e}_1$, $\mathbf{e}_2$ and $\mathbf{e}_3$ with $|\mathbf{e}_1| = |\mathbf{e}_3| = 1$ and $|\mathbf{e}_2| = |\mathbf{e}_4| = \rho$. The angles α and β are defined as $(\mathbf{e}_1, \mathbf{e}_3) = 2\alpha$ and $(\mathbf{e}_1, \mathbf{e}_2) = \alpha + \beta$. The structure has the space group $p2$ whereas the $\mathbb{Z}$-module is the projection of the four-dimensional lattice of space group *pmm*.

$$\begin{aligned} &Cmcm(A_O, B_O, C_O) \\ &= \{(1|000) + (1|001)\} \\ &\quad \times \{(1|000) + (m_x|000) + (m_y|00\tfrac{1}{2}) + (2_z|00\tfrac{1}{2})\} \\ &\quad \times C1m1(2A_O, 2C_O, -1/2(A_O + B_O)) \end{aligned}$$

expressed on the *Cmcm* basis. This shows that, in the monoclinic phase, we should observe four types of orientational variants times two types of translational variants, a total of eight variants which all share the same reciprocal lattice for even k. This explains the complexity of planar defects observed by TEM compared with the relative simplicity of the diffraction patterns.

Initially described in *Cmcm* by the Wyckoff positions 4*c*: $0, y, \frac{1}{4}$ and $0, \overline{y}, \frac{3}{4}$, for each Ni and Zr atomic species, the structure in $C1m1$ is described with the new Wyckoff positions

$$x_M = \frac{1}{2}(x_O - y_O),\ y_M = \frac{1}{2}z_O,\ z_M = -2y_O.$$

Explicitly for the present case $x_M = -y/2$, $y_M = 1/8$, $z_M = -2y$ so that we end up with the crystal description using the template[6] for the two atomic species:

$$\begin{array}{llll} w_1 = & -x_M & 0 & -z_M \\ w_2 = & x_M & \beta/4 & z_M \\ (w_2' = & x_M & -\beta/4 & z_M) \\ w_4 = & -x_M & 1/2 & -z_M \end{array}$$

where we have translated the origin for $C1m1$ along the *b* axis by 1/8 to select it on the pure mirror perpendicular to the *b* axis (the *c* axis of the *Cmcm* structure). Here, β is equal to 1 in the orthorhombic structure and can take any value in the monoclinic one.

[6] In our case of the NiZr alloy, the values of x_M and z_M are the following: $x_{Zr} = 0.18045$, $z_{Zr} = 0.7218$, $x_{Ni} = 0.04085$, $z_{Ni} = 0.1634$ (and, of course, $\beta = 1$ for the ideal *Cmcm* structure).

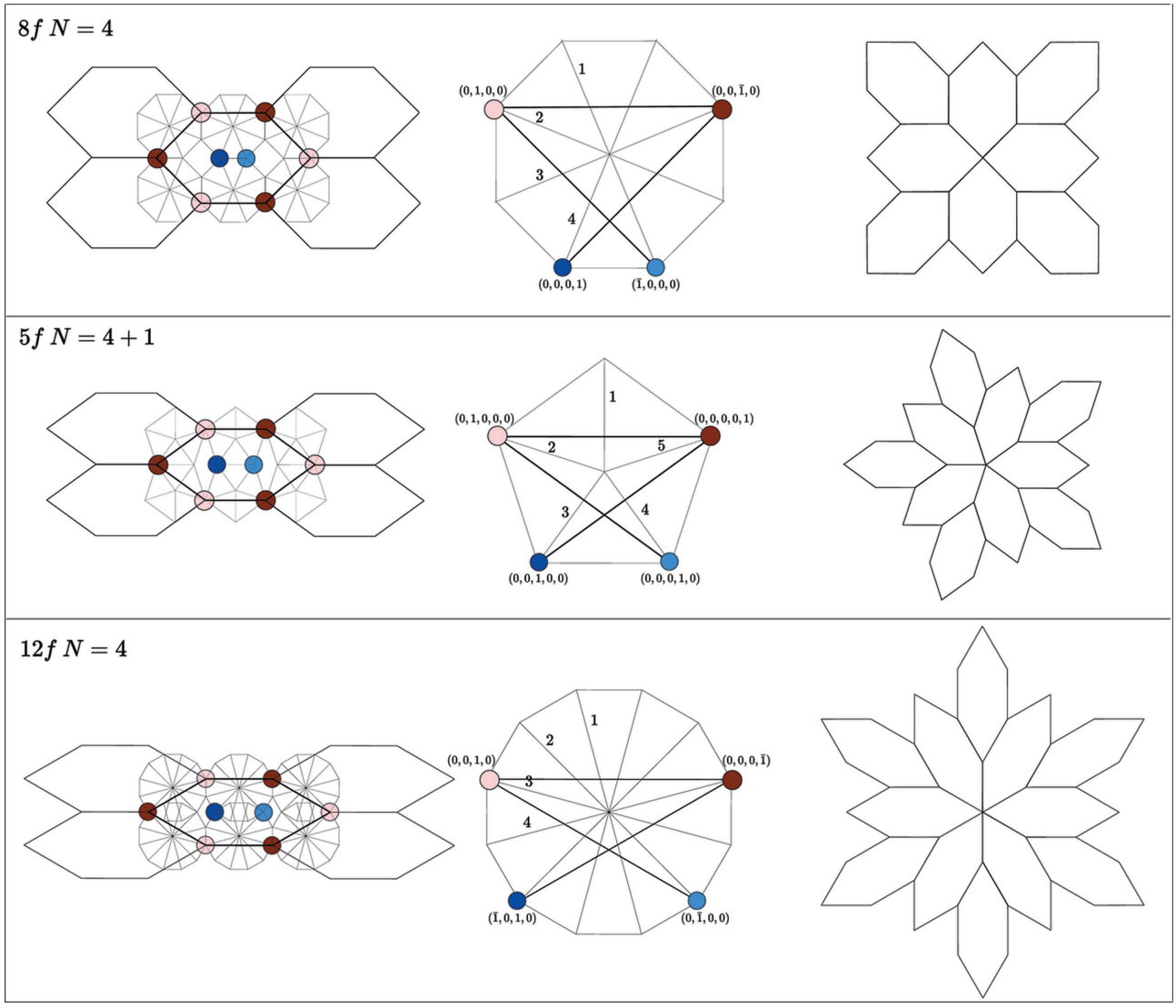

Figure 17
Interesting specific cases appear for the CrB-type structure where $\rho = 1$ if $\alpha = \pi/K$, $K \in \mathbb{Z}^+$. On top, the case $K = 8$ generates octagonal twins that are described using a $\mathbb{Z}$-module of rank 4 defined by the four vectors 1, 2, 3 and 4 in the very same way as the pentagonal module ($K = 10$) of NiZr. The case of $K = 12$ leading to dodecagonal twins is also very simple to handle since the corresponding $\mathbb{Z}$-module is also of rank 4. Unit cells are: octagonal $A = (\bar{1}, \bar{1}, 1, 1)$, $B = (1, 3, 3, 1)$; dodecagonal $A = (\bar{1}, \bar{1}, 0, 1)$, $B = (\bar{1}, 1, 4, 3)$ [see Hornfeck *et al.* (2014) Fig. 7 for an illustration of chiral twins of the CrB type with octagonal and dodecagonal symmetry].

The diffraction amplitude $F(h, k, l)$ expressed in the reciprocal lattice of the monoclinic structure is easily calculated. Let us put $\alpha(x, z) = 2\pi(hx + lz)$:

$$F(h,k,l) \propto \Big\{\exp[-i\alpha(x,z)][1+\exp(i\pi k)] + \exp[i\alpha(x,z)] \times \Big[\exp\Big(-i\frac{\pi}{2}\beta k\Big) + \exp\Big(i\frac{\pi}{2}\beta k\Big)\Big]\Big\} \times \{1+\exp[i\pi(h+k)]\}$$

or

$$F(h,k,l) = 2\Big\{\exp[-i\alpha(x,z)][1+\exp(i\pi k)] + 2\exp[i\alpha(x,z)]\cos\frac{\pi}{2}\beta k\Big\}$$

with $h + k = 2n$.

The first term vanishes for odd k and the second one vanishes for odd k and $\beta = 1$ (*i.e.* in the *Cmcm* structure). These extinctions are independent of the value of $\alpha(x, z)$. This shows that the monoclinic structure is the derivation of the CrB-type structure where $\beta \neq 1$, *i.e.* where the atoms generated by w_2 and w_2' are (slightly) displaced along the y direction of the monoclinic phase, *i.e.* the z direction of the CrB-type structure.

In summary, the case $\beta = 1$ generates the diffraction pattern corresponding to the standard CrB *Cmcm* structure whereas $\beta \neq 1$ generates the diffraction corresponding to the monoclinic distorted structure with half of the atoms of Ni(Zr) (slightly) displaced along the z direction of the CrB structure as shown in Fig. 15.

The most important result with respect to the main purpose of the present article is twofold:

(i) Whatever structure, orthorhombic or monoclinic, is actually observed in the microscope, there are no differences in the HREM and HAADF images if observed along the [001] direction (orthorhombic indexing).

(ii) Whatever the actual value of the parameter β in the monoclinic phase, the five-dimensional scheme used here remains perfectly valid.

APPENDIX *B*
A generalization of coherent mirror twins

The case of the quinary twin generated by a $[1, \overline{1}, 0]$ mirror can be generalized to many structures outside those of the CrB type. In fact, this happens each time the structure has the property of being possibly described as a two-dimensional tiling of identical hexagonal tiles where the hexagon has two adjacent sides of equal length as exemplified in Fig. 16 (Bouzy, private communication). There, the coherent twin is easily defined using the four-dimensional $\mathbb{Z}$-module generated by the four vectors $\mathbf{e}_1$, $\mathbf{e}_2$, $\mathbf{e}_3$ and $\mathbf{e}_4$, where $\mathbf{e}_3$ and $\mathbf{e}_4$ are mirrors of, respectively, $\mathbf{e}_1$ and $\mathbf{e}_2$. Choosing $|\mathbf{e}_1|$ as the length unit, we define $\rho = |\mathbf{e}_2|$, $2\alpha = (\mathbf{e}_1, \mathbf{e}_3)$ and $\beta = (\mathbf{e}_1, \mathbf{e}_2) - \alpha$. The two-dimensional unit cell is defined by $A = (1, 0, 1, 0)$ and $B = (\overline{1}, 1, 0, 0)$ with space group $p2$. The projection matrix (not normalized) into the physical space is thus

$$\widehat{\mathbf{\Pi}}_\alpha = \begin{pmatrix} \cos\alpha & \rho\cos\beta & \cos\alpha & \rho\cos\beta \\ -\sin\alpha & \rho\sin\beta & \sin\alpha & -\rho\sin\beta \end{pmatrix}.$$

The four-dimensional lattice generating the $\mathbb{Z}$-module has space group pmm' with $m = \{3, 4, 1, 2\}$ and $m' = \{-3, -4, -1, -2\}$ so that the coset decomposition of pmm' onto $p2$ with the same lattice gives two variants, *i.e.* one twin characterized by the mirror $\widehat{\mathbf{m}} = (\{3, 4, 1, 2\}|1000)$ and its associated translation $\mathbf{t}$ decomposes into $\mathbf{t}_i = 1/2(1, 0, 1, 0) = \mathbf{A}/2$ and $\mathbf{t}_r = 1/2(1, 0, \overline{1}, 0)$. The translation $\mathbf{t}$ can be expressed in the unit cell of the transformed variant as $\mathbf{t} = \{0, 1/[2(1 + \cos 2\alpha)]\}$. Fig. 17 shows, beyond the pentagonal case, the two special high-symmetry cases of octagonal and dodecagonal systems, both modules of rank 4, where easy coherent twins are expected to occur.

Acknowledgements

The authors are very grateful to the other members of the DLR team, W. Hornfeck and M. Kolbe, for their help in NiZr sample characterization and preparation, as well as for discussions regarding the development of the chiral decagonal twin model as published in Hornfeck *et al.* (2014), which led to the current investigations on NiZr. We thank Professor Emmanuel Bouzy for the discussions that are the basis of Appendix *B*. The authors acknowledge the efficient help of Dominique Lamirault (CEMES) and Julie Bourgon (ICMPE) in the sample preparations for electron microscopy observations.

Funding information

The acquisition of the STEM-HAADF and STEM-BF ultra-high-resolution pictures using the TITAN electron microscope (C2N) was made possible with the financial help of the project Equipex TEMPOS ANR-10-EQPX-50. Finally, this work and the doctoral position of one of us (A. Sirindil) has been financially supported by the French ANR under project ANR METADIS 13-BS04-0005 which is gratefully acknowledged.

References

Bendersky, L. A., Stalick, J. K., Portier, R. & Waterstrat, R. M. (1996). *J. Alloys Compd*, **236**, 19–25.

Bouzy, E., Caër, G. L. & Bauer-Grosse, E. (1991). *Philos. Mag. Lett.* **64**, 1–6.

Duneau, M. & Katz, A. (1985). *Phys. Rev. Lett.* **54**, 2688–2691.

Elser, V. (1986). *Acta Cryst.* A**42**, 36–43.

Gratias, D., Katz, A. & Quiquandon, M. (1995). *J. Phys. Condens. Matter*, **7**, 9101–9125.

Hirth, J. P. & Pond, R. C. (1996). *Acta Mater.* **44**, 4749–4763.

Hornfeck, W., Kobold, R., Kolbe, M. & Herlach, D. (2014). arXiv: 1410.2952.

Jarić, M. V. & Mohanty, U. (1987). *Phys. Rev. Lett.* **58**, 230–233.

Jiang, W. J., Hei, K., Guo, Y. X. & Kuo, K. H. (1985). *Philos. Mag. A*, **52**, L53–L58.

Kalugin, P. A., Kitaiev, A. Y. & Levitov, L. S. (1985). *JETP Lett.* **41**, 145–147.

Kirkpatrick, M. E., Bailey, D. M. & Smith, J. F. (1962). *Acta Cryst.* **15**, 252–255.

Parthé, E. (1976). *Acta Cryst.* B**32**, 2813–2818.

Penrose, R. (1979). *Math. Intelligencer*, **2**, 32–37.

Pond, R. C. (1989). In *Dislocations in Solids*, Vol. 8, edited by F. R. N. Nabarro. Amsterdam: North Holland.

Quiquandon, M., Gratias, D., Sirindil, A. & Portier, R. (2016). *Acta Cryst.* A**72**, 55–61.

Shechtman, D., Blech, I., Gratias, D. & Cahn, J. W. (1984). *Phys. Rev. Lett.* **53**, 1951–1953.

Sirindil, A., Quiquandon, M. & Gratias, D. (2017). *Acta Cryst.* A**73**, 427–437.